Recovery of Optical Transport Coefficients Using the Diffusion Approximation in Bilayered Tissues: A Theoretical Analysis

Suraj Rajasekhar and Karthik Vishwanath *

Posted Date: 23 May 2025

doi: 10.20944/preprints202505.1896.v1

Keywords: Time resolved diffuse reflectance; Time domain transport; NIRS; Spectroscopy; Diffusion Approximation

 doi:10.20944/preprints202505.1896.v1

Article

Recovery of Optical Transport Coefficients Using Diffusion Approximation in Bilayered Tissues: A Theoretical Analysis

Suraj Rajasekhar [1] and Karthik Vishwanath [1,2,*,†]

[1] Cellular, Molecular and Structural Biology Program, Miami University, 501 E High Street, Oxford, Ohio 45056
[2] Department of Physics, Miami University, 500 E Spring Street, Oxford, Ohio 45056
* Correspondence: vishwak@miamioh.edu
† Current address: Department of Physics, Miami University, 500 E Spring Street, Oxford, Ohio 45056.

Abstract: Time-domain (TD) diffuse reflectance can be quantified using photon diffusion theory (DT) to non-invasively obtain optical transport coefficients of biological media, which in turn provide markers of tissue physiology. We use an optimized, N-layer numerical DT solver in cylindrical geometry to recover optical coefficients of bi-layered media using time-resolved reflectance generated by Monte Carlo (MC) simulations. Optical coefficients for each layer of 384 bilayered tissue models were obtained from literature to model human head or limb tissue, at three near-infrared wavelengths. We fit MC data using a layered DT model to reconstruct transport coefficients of both layers simultaneously. We could retrieve bottom-layer absorption with errors less than 0.02 cm^{-1} while top-layer scattering was recovered to 3 cm^{-1} of input values. Reconstructions of the bottom-layer scattering had a mean error greater than 50%. Total hemoglobin concentration and fractional oxygen saturation were reconstructed in both layers and were within 10 μM and 5%, respectively, for the bottom layer. Recovered values of transport coefficients were significantly improved with the layered DT compared to the more widely used semi-infinite DT. Findings suggest that incorporating layered models in fitting TD reflectance could enhance its value in applications.

Keywords: time resolved diffuse reflectance; time domain transport; NIRS; spectroscopy; diffusion approximation

1. Introduction

Time domain diffuse optical spectroscopy (TD-DOS) is a quantitative, non-invasive technique that has been widely explored across several biomedical applications [1–5]. The quantitative nature of this technique relies on recovering the wavelength-dependent transport coefficients –the absorption coefficient $\mu_a(\lambda)$ and the reduced scattering $\mu_s'(\lambda)$ to optically characterize the medium from which measurements are obtained. In TD-DOS, the measured temporal attenuation and broadening of an input source (which experimentally is usually a laser having pulse durations of 10-100 ps) is mathematically modeled using theoretical or numerical methods to recover the optical coefficients $\mu_a(\lambda)$ and $\mu_s'(\lambda)$ [6–10]. In human tissues, accurate recovery of $\mu_a(\lambda)$ at multiple wavelengths allows for reconstructions of component chromophore concentrations such as hemoglobin, water, and/or lipids, while $\mu_s'(\lambda)$ is influenced by tissue microstructure [6,9,11–14]. These chromophore concentrations are used to estimate tissue vascular oxygen saturation, total blood volume, hydration, and/or cellular density *in vivo* [15–17].

Theoretical models are critical for recovering optical transport coefficients from measurements, as they provide the quantitative platforms to model light transport in turbid media. A commonly used theoretical approach to quantify TD-DOS measurements is diffusion theory (DT)[18–22]. DT-based approaches typically consider the tissue medium as optically-homogeneous and semi-infinite in extent across in various applications, including tracking and monitoring cerebral oxygenation

 doi:10.20944/preprints202505.1896.v1

and cancer development in clinical settings [3,8,19,23,24]. Though modeling biological tissues as a semi-infinite homogeneous medium allows for quantitative analysis, it is inherently insensitive to any inhomogeneities of the medium, which has been shown to lead to large errors in recovering physiological parameters [6,7,9,25–27].

Representing tissue as a bilayered medium would be more realistic than as a semi-infinite medium –e.g., a human head can be better modeled as having a top layer (representing scalp and skull) and a bottom layer (for the cerebral spinal fluid, gray and white matter) and limb tissues can be modeled as a layer of muscle buried under a upper-layer of fat and skin [6,28]. The use of layered models in DT would permit reconstruction of optical coefficients for each layer, independently, from the measured TD reflectance [11,17,29]. Bilayered models can thus naturally detect transport coefficients of deeper layers better, and could also be used to suppress cross-talk from superficial layers [21,30,31]. Such depth-dependent reconstructions would enhance the accuracy of cerebral and muscular hemodynamic assessments [29,30,32–35].

Analytical solutions of TD reflectance using DT in bilayered media have been reported previously [18,36–39]. However, they are not commonly used as the implementation of these solutions require computing complex analytical expressions that often include hyperbolic functions, leading to numerical instabilities because of finite machine-precision. Thus, these solvers have high computational complexity and costs [7,35,40–43]. Recently, we have developed an easy-to-use, open-source library - lightPropagation.jl - that is numerically stable and highly optimized (with a single calculation for a forward solution taking less than 0.5 ms on standard laptop computers) for computing time domain reflectance in multilayered tissue models via DT [44].

Here, we seek to establish the accuracy and precision of using lightPropagation.jl for inverse reconstruction of optical coefficients using time-domain reflectance acquired from using Monte Carlo (MC) simulated of time-resolved reflectance in bilayered tissue models. We assess the performance of the inverse model in recovering the absorption and reduced scattering coefficients. To ensure appropriate relevance to biomedical applications, we selected optical properties for tissue models simulated to match values reported in literature [28]. We use wavelength-dependent reconstructions to derive functional biological markers of fractional oxygen saturation (SO_2) and hemoglobin concentrations for each tissue layer and quantify the errors associated with reconstructions to establish limits for accuracy and precision of recovered optical coefficients and functional endpoints.

2. Materials and Methods

2.1. Bi-Layered Tissue Models

Two types of tissue models, representing head and limb muscle tissue were used to generate TD reflectance using MC simulations and are depicted by Figure 1(a). Both tissue models were represented as cylinders with large radius (set to 100 cm), had upper layer thickness of 1 cm, and had semi-infinite bottom layer (thickness of 100 cm) to compute MC and DT solutions. Input values of the absorption coefficient for each layer in each tissue model was determined by solely by two chromophores - oxygenated ([HbO]) and deoxygenated hemoglobin ([dHb]) [45]. Table 1 lists values for inputs used to generate optical coefficients in each layer, for each tissue model.

Eq.(1) was used to determine μ_a for each layer by specifying values for $[THb]$ and SO_2 and using molar extinction coefficients $\epsilon_{HbO}(\lambda)$ and $\epsilon_{dHb}(\lambda)$ from literature [28,46]. The reduced scattering coefficients (μ_s') for the top and bottom layer were calculated using Eq.(2) using literature values for A and b, for each layer and tissue type [12,28].

$$\mu_a(\lambda) = SO_2 \cdot (\epsilon_{Hbo}(\lambda) \cdot THb + \epsilon_{dHb}(\lambda) \cdot (1 - THb)) \tag{1}$$

$$\mu_s'(\lambda) = A\left(\frac{\lambda}{500}\right)^{-b} \tag{2}$$

 doi:10.20944/preprints202505.1896.v1

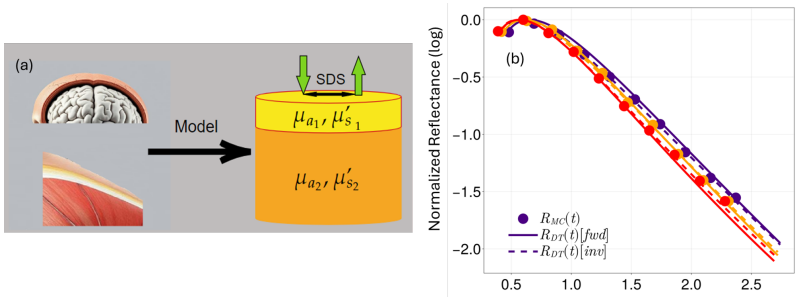

Figure 1. (a) illustrates two-layer models for head and limb tissues. Each layer is represented as a cylinder having the same radius, but different thickness. All models used had fixed upper layer thickness of 1 cm. Tissue media were characterized the absorption (μ_{a_1}, μ_{a_2}) and reduced scattering coefficients (μ'_{s_1}, μ'_{s_2}), where layer 1 was the top layer. **(b)** time-resolved reflectance from a muscle tissue model obtained using MC (symbols), forward DT calculations (solid lines) and from inverse-fits (dashed lines) at SDS = 1.5 cm. Colors represent data for the same tissue model at three wavelengths used (indigo: 690 nm, orange: 760 nm and red: 850 nm).

Table 1. Input parameters used to generate optical coefficients of each layer. Two $[THb]$ and SO_2 values were used for the top and bottom layers, along with two different values of A and b for the top and bottom layers. A total of 64 different models were generated at any one wavelength.

Tissue Model	**Layer**	$THb(\mu M)$	$SO_2(\%)$	$A(cm^{-1})$	b
Head	Top	$[31.0, 75.0]$	$[60, 98]$	$[21.4, 40.8]$	$[1.200, 3.100]$
	Bottom	$[33.0, 65.0]$	$[55, 70]$	$[9.5, 20.9]$	$[0.141, 0.537]$
Muscle	Top	$[18.0, 61.0]$	$[50, 90]$	$[23.7, 35.2]$	$[0.385, 0.988]$
	Bottom	$[27.0, 50.0]$	$[50, 69]$	$[13.0, 9.8]$	$[0.920, 2.800]$

64 different models were generated at three commonly used near infrared wavelengths (690, 760, and 850 nm) to span the isosbestic points of hemoglobin [6,14,20]. The full dataset consisted of 384 $(64 \times 3 \times 2)$ bilayered tissue models, on which we conducted the analysis. Ranges for optical coefficients at each of the three wavelengths used, for each layer, are listed in tables A1, A2 and A3 for 690 nm, 760 nm and 850 nm, respectively.

2.2. Monte Carlo Simulation of Reflectance Signals

A previously used Monte Carlo code for photon transport was used to simulate time-resolved reflectance from each of the 384 tissue models [47,48]. MC simulations for all models were computed with 3×10^8 photons. For each simulation, the input source was a pencil beam (representing a delta-function) incident at the origin of the tissue model and the TD diffuse reflectance was recorded between 1cm to 3 cm in intervals of 0.25 cm with timing relative to the input delta-function source. Reflectance data was stored between $0 - 7$ ns with temporal resolution of 0.01 ns simulations were run on a high-performance computing cluster (with each node of the cluster hosting Intel Xeon Gold processors). Each MC simulation required about 15 hours to execute and simulations were run in parallel (on separate compute nodes) to increase output efficiency. For analysis, each simulated time-resolved reflectance was smoothed (using a moving-window of span 5 or a temporal window of 0.05 ns), normalized (peak intensity = 1), truncated (by retaining values greater than 80% of peak intensity of the rising edge to eliminate early arriving photons and lesser than than 10^{-3}% of the tail to limit statistical noise), and lastly log-transformed to obtain $R_{MC}(\rho, t)$. Although we simulated reflectance data between 1-3 cm, we only use reflectance at three specific source detector separations (SDS) of 1.5, 2 & 2.5 cm because the noise in MC simulations at SDS of 3 cm was too high for use here.

2.3. Forward-Modeling of Diffuse Reflectance Signal

The numerical DT solver lightPropagation.jl was used to obtain the TD-reflectance (the temporal point spread function or TPSF), for any given bilayered cylindrical tissue model [27]. The SDS and

 doi:10.20944/preprints202505.1896.v1

was set to match those from the MC simulations, the refractive index of each layer was fixed to be 1.4 which is consistent for biological tissues from previous work [49] and the top layer thickness was set to 1 cm. To compute the reflectance signal, for each tissue model required inputs for the four transport coefficients, μ_{a_1}, μ_{a_2}, μ'_{s_1} and μ'_{s_2}. The computed signal was was then truncated, normalized and log-transformed following the same protocol used for processing the MC reflectance signal, to obtain $R_{DT}(t)$.

Figure 1(b) shows representative data for TD-reflectance simulated (in symbols) and predicted from DT (solid lines) at three different wavelengths (colors) for a muscle tissue model. The values of optical absorption and scattering were calculated at each wavelength using Eq.(1) and Eq.(2) where $[THb]$ was 18μM for the top layer and 27μM and for bottom layer, with both layers having SO_2 of 50%.

2.4. Inverse Fitting of Reflectance

Inverse modeling sought to recover the four optical transport coefficients (the absorption and scattering for each layer) by fitting each time-resolved reflectance $R_{MC}(t)$, at each SDS, for each of the 384 tissue models. Fits were obtained iteratively using a Levenberg-Marquardt non-linear optimizer (LVM) (LsqFit package in Julia version 1.9.1) to compute a set of inputs to compute $R_{DT}(t)$ that best matched the input $R_{MC}(t)$. For DT calculations, the top layer thickness was assumed to be known (kept fixed for all analysis here at 1 cm), the refractive indices of both layers were held fixed at 1.4 and the SDS was set to match $R_{MC}(t)$. During optimization the optical coefficients were constrained to be bounded between $0.01 < \mu_a < 0.5$ for absorption and between $2 < \mu'_s < 30$ for scattering.

A normalized mean absolute error (ζ) value was computed to evaluate goodness of fits between $R_{DT}(t)$ and $R_{MC}(t)$ using equation 3

$$\zeta = \frac{\text{MAE}}{\overline{|R_{MC}(t)|}} \tag{3}$$

Here, $\overline{|R_{MC}(t)|} = \frac{1}{N}\sum_{i=1}^{N}|R_{MC}(t_i)|$ represents the average of the absolute value of the reflectance signal, and $\text{MAE} = \frac{1}{N}\sum_{i=1}^{N}|R_{MC}(t_i) - R_{DT}(t_i)|$. N represents the total number of time bins in $R_{MC}(t_i)$ and $N \approx 180 \pm 100$ across the entire data-set, due to data truncation of $R_{MC}(t)$ that was noted above.

For each simulated reflectance $R_{MC}(t)$, inverse fitting was repeated until $\zeta \leq 0.03$. If ζ was higher than this after 25 attempts the solution with lowest ζ was used as the fit. In Figure 1(b) inverse fits are shown by dashed lines and had $\zeta = 0.017, 0.015$ & 0.018 for 690 nm (indigo), 760 nm (orange) and 850 nm (red) models, respectively.

Lastly, we also used the semi-infinite DT approximation to fit $R_{MC}(t)$ using lightPropagation.jl [27]. The forward fitting used in lightPropagation.jl replicates the expression for semi-infinite DA reflectance in Ref.[37]. Inverse fitting for the semi-infinite model mirrored the bilayered approach, and used the optimizer algorithm to extract two coefficients μ_a and μ'_s to the same goodness-of-fit threshold as used in the bi-layer reconstructions ($\zeta = 0.03$) and used the same search ranges for each optical coefficient ($0.01 < \mu_a < 0.05; 2 < \mu'_s < 30$).

2.5. Retrieval of Functional Endpoints

As most real-world applications of TD-DOS involve extracting tissue physiological parameters from optical coefficients we emulated that process to the reconstructed absorption coefficients at multiple wavelengths to obtain the functional parameters of $[dHb]$ and $[HbO]$ using 4

$$\begin{bmatrix}\mu_a(\lambda_1)\\ \mu_a(\lambda_2)\\ \mu_a(\lambda_3)\end{bmatrix} = \begin{bmatrix}\epsilon_{HbO}(\lambda_1) & \epsilon_{dHb}(\lambda_1)\\ \epsilon_{HbO}(\lambda_2) & \epsilon_{dHb}(\lambda_2)\\ \epsilon_{HbO}(\lambda_3) & \epsilon_{dHb}(\lambda_3)\end{bmatrix}\begin{bmatrix}[HbO]\\ [dHb]\end{bmatrix} \tag{4}$$

Here, values of $[dHb]$ and $[HbO]$ were estimated using the same optimizer (as used for TD-reconstructions) to ensure only non-negative values of $[dHb]$ and $[HbO]$ were allowed as solutions by the optimizer. This eliminated any solutions with negative values for concentrations and thus

 doi:10.20944/preprints202505.1896.v1

remain physiologically meaningful. The chromophore concentrations were used to compute $[THb]$ (as $[dHb]$+$[HbO]$) and fraction SO_2 (as $[HbO]/[THb]$) which were each then compared to input values used for each model (shown in Table 1). This process was repeated for each SDS.

3. Results

The inverse fitting protocol was employed to recover optical coefficients from each of the 384 MC models at three SDS. Reconstructions for the absorption (μ_{a_1}, μ_{a_2}) and reduced scattering coefficients ($\mu's_1$, $\mu's_2$) at 760 nm are shown in Figure 2. The mean goodness of fits at 1.5 cm and 2 cm had $\zeta \leq 0.01$, across all models, with head reconstruction performing marginally better (average ζ(head) was 0.005 lesser than ζ(muscle)). However, for SDS of 2.5 cm, ζ increased to 0.02 which we hypothesize was due to an increase in statistical noise in the MC simulations at longer SDS. Each iteration for convergence took approximately 15 s on average and most $R_{MC}(t)$ fits needed $10-15$ iterations to meet the required convergence threshold. In Figure 2 each marker corresponds to some fixed value for the optical coefficient being plotted, while the other three coefficients were varied. For instance, each marker in Figure 2(a) is from 16 different tissue models that shared the same μ_{a_1} value, while error bars are the standard error across all those 16 reconstructed values of μ_{a_1} as μ_{a_2}, μ'_{s_1} and μ'_{s_2} were permuted.

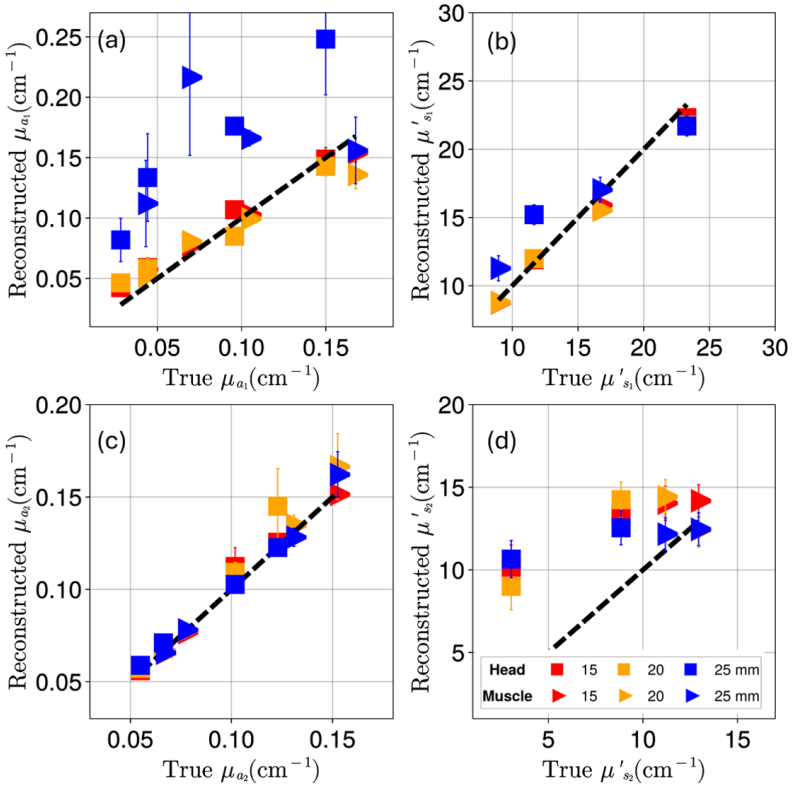

Figure 2. True versus reconstructed optical coefficients at 760 nm for absorption (μ_{a_1} and μ_{a_2} in **(a)** and **(c)**) and reduced scattering coefficients (μ'_{s_1}, μ'_{s_2} in **(b)** and **(d)**) across each of the 64 models for brain (squares) and the 64 models for muscle (triangles). Colors represent different SDS: red for 1.5cm, orange for 2 cm and blue for 2.5 cm and the dashed black line represents the $y = x$ line. The error bars represent the standard error across all models that share fixed values of each optical coefficient under investigation. It is important to note that there are six different markers each with its own error bar. Many of the error bars are smaller than the marker sizes used.

Figure 2(d) clearly show that the largest reconstruction errors were seen bottom layer scattering μ'_{s_2} with reconstruction errors, generally $> 5cm^{-1}$ for all SDS. The difficulty of layered DT in reconstructing deep-layer scattering estimation observed here has been reported previously [18,50,51]. Recovery of μ_{a_1} was inconsistent and showed significant errors for some of the tissue models tested but the mean reconstruction error was lower than $0.03cm^{-1}$ at SDS $=$ 1.5 cm and 2 cm, with good agreement in many cases, as noted in Figure 2(a) by the overlapping markers. Larger errors in reconstructed values for

 doi:10.20944/preprints202505.1896.v1

μ_{a_1} were noted at SDS of 2.5 cm growing to nearly $0.1cm^{-1}$. Recovery of μ_{a_2} and μ'_{s_1} were the highly accurate with errors < 0.01 and $< 2\ cm^{-1}$, respectively, for all SDS tested. These trends preserved at the other two wavelengths (Supplementary Figures A1 for 690 nm and Figures A2 for 850 nm)

The impact of reconstruction errors on derived physiological parameters was next investigated by computing the reconstructed concentrations of ($[dHb]$) and ($[HbO]$), as illustrated in Figure 3. Reconstructed absorption coefficients at 690 nm, 760 nm, and 850 nm were used to derive the hemoglobin concentrations. Due to the sparse and non-uniform distribution of hemoglobin concentrations used in simulated tissue models, the x-axis are scaled to reflect the actual concentration values and thus the values from bar heights need to interpreted in conjunction with their x-axis locations, to assess performance of reconstructions.

Results in Figure 3(a) and 3(b), demonstrate that top-layer hemoglobin retrieval was less accurate than reconstructions in the bottom layer. Most of the reconstructed values in the upper layer either overestimated (for smaller values of $[dHb]$) or underestimated (for larger values of $[dHb]$). For instance, the reconstructed value for $[dHb]$ was $6 \pm 1\mu$M when its true value was 1.8μ M for muscle (the third bar in Figure 3(a)). However, the spread (standard error) remained within 10μM across all models which is sufficient for clinical use [52]. The reconstructions for bottom-layer concentrations were accurate overall, with reconstructed values for both $[dHb]$ and $[HbO]$ being well within the computed standard error (Figures 3(c) and 3(d)). This trend was true at all SDS used, but data at larger SDS were associated with a larger spread in reconstructed values.

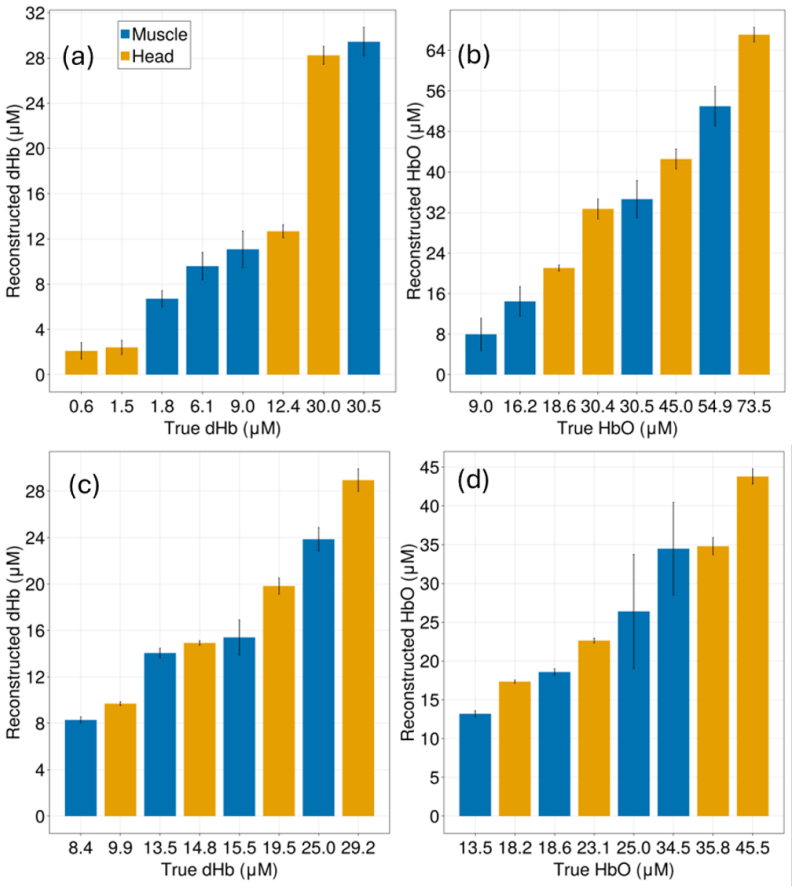

Figure 3. Reconstructed $[dHb]$ and $[HbO]$ concentrations for muscle (blue) and brain (orange) at an SDS of 1.5 cm. The x-axis represents the true hemoglobin concentrations (not evenly spaced) computed from the model values derived from 1. While the y-axis shows the reconstructed (median) values. Subplots **(a)** and **(b)** represent the top layer and **(c)** and **(d)**, the bottom layer reconstruction of $[dHb]$ and $[HbO]$ respectively. Each data bar in each plot represents sixteen models and the error-bar is the standard error across the models.

 doi:10.20944/preprints202505.1896.v1

Functionally, the most common biomarkers sought by real-world applications using TD-DOS include the total hemoglobin concentration $[THb]$ and fractional oxygen saturation SO_2 which are computed using wavelength-dependent optical transport coefficients. Figure 4 shows the true (input) values used for SO_2 and total hemoglobin concentration $[THb]$ values for the top and bottom layers vs. those derived from the inverse DT. As expected and seen in the figures, errors in hemoglobin concentrations of the top layer directly affect the accuracy of the derived physiological markers of SO_2 and $[THb]$, leading to significant deviations from their true values.

These appear as incorrect median reconstructed values as well as higher standard error all SDS. However, both precision and accuracy of reconstructed values for the bottom layer (Figures 4(c) and 4(d)) were excellent with the reconstructed median values of both SO_2 and $[THb]$ matching the expected physiological ranges to better than 3% across all SDS. One exception to this was seen for muscle models where $[Thb] = 50\mu$M and $SO_2 = 50\%$ (for the bottom layer) that exhibited large standard error in derived values (the median value was in agreement to the true value to within 3% again) . These same tissue models shown in Figure 3 also had large standard errors in reconstructed $[dHb]$ and $[HbO]$ concentrations.

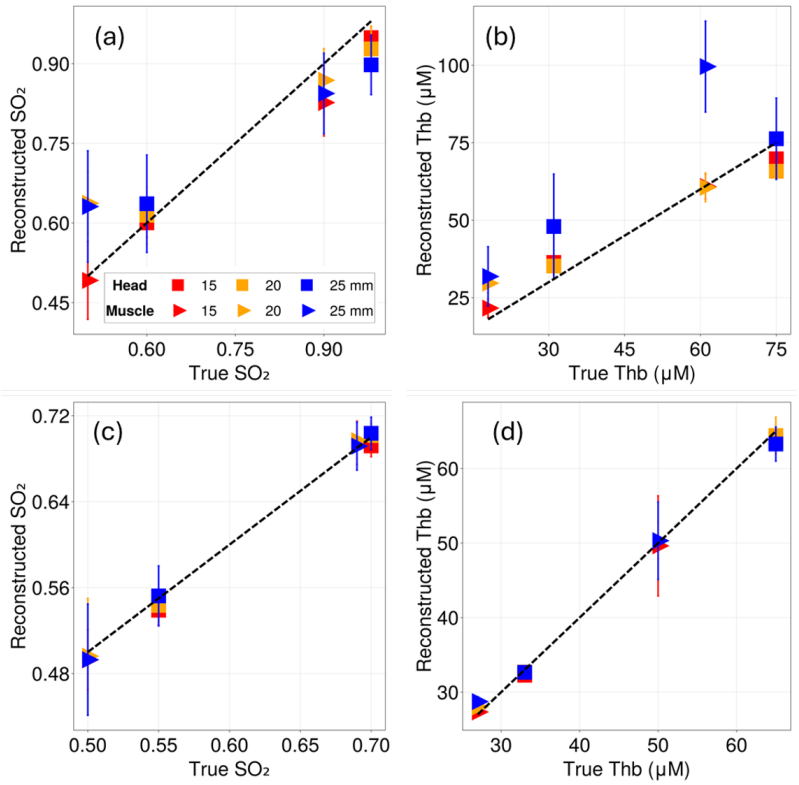

Figure 4. Reconstruction accuracy of SO_2 and $[THb]$ for different source-detector SDS in a two-layer model. **(a)** and **(b)** show the reconstructed (median) versus true values of SO_2 and $[THb]$, respectively, for the top layer, while **(c)** and **(d)** display the same for the bottom layer. The colors represent different SDS values: 1.5 mm (red), 2 mm (orange), and 2.5 mm (blue). The dash black line represents the $y = x$ line. The reconstruction for the top layer showed poor accuracy while the bottom layer reconstruction showed much better reconstructions, highlighting the effectiveness of DT to probe deeper tissue layers. These data were computed using reconstructed $[dHb]$ and $[HbO]$ values.

As a final point of analysis, we reconstructed optical coefficients from the bilayered $R_{MC}(t)$ using the semi-infinite DT expression for TD reflectance. Since the SI model reconstructed optical coefficients for a homogeneous model (hence only recovers two optical coefficients), we compared the recovered absorption coefficient to both μ_{a_1} and μ_{a_2} and repeated that for the reduced scattering as well. Figure 5, shows the median percent error (bars) along with the standard error (error bars) for all MC models (head and tissue) simulated at 15 mm SDS. It is clear that even with the difficulties in reconstruction of

 doi:10.20944/preprints202505.1896.v1

four optical coefficients using bi-layer DT models, the retrieved layer specific transport coefficients were always more accurate than those estimated by the semi-infinite model with a notable exception for retrieval of μ'_{s_2}. This is also true for SDS $=$ 2 cm but at SDS $=$ 2.5 cm, the reconstruction of μ_{a_1} was significantly affected (Figure A5)

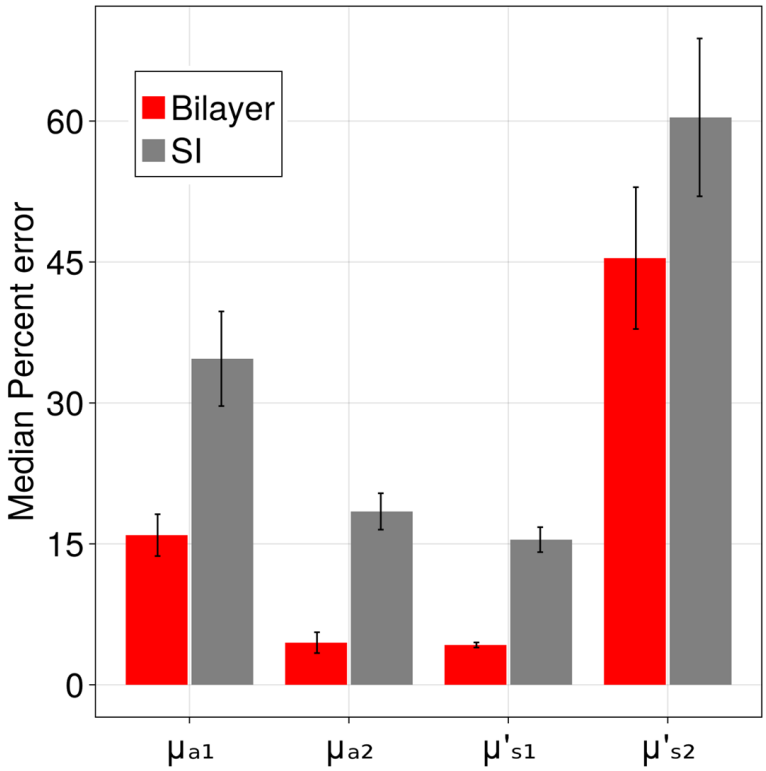

Figure 5. Comparison of median percent error in reconstructed transport coefficients of bilayered media using a semi-infinite DT model. Each orange bar represents the median percent error in reconstructed absorption and scattering obtained from inverse SI DT model across the 384 bi-layered while the true value for each of the four coefficients (indicated by the axis labels) were those used to simulate $R_{MC}(t)$. Error bars indicate the standard errors across the 384 models. The blue bars indicate these errors when reconstructions were done by using bilayered DT.

4. Discussion

We verified the accuracy of a recently reported, open-source, numerical solver of DT in cylindrical coordinates, lightpropagation.jl, to function as an inverse solver in bilayer tissue models using TD reflectance simulated at multiple SDS. 384 bilayered models were simulated using MC for a range of tissue optical properties that have been reported for head and muscle tissues. The goodness of fit was established by computing the Normalized Mean Absolute Error (ζ), which on average was (across all models) lower than 0.01 at SDS $=$ 1.5 and 2 cm while $\zeta \geq 0.02$ at SDS of 2.5 cm. A change of 0.01 in ζ in goodness of fit significantly impacted accuracy of reconstructions of the top layer absorption μ_{a_1} as seen in Figure 2(a) (and Figures A1(a) A2(a)). Thus ζ could potentially signal a measure of confidence in the retrieved value of optical coefficients for each fitted reflectance and could also serve as a measure of signal quality in experimental use.

A threshold of $\zeta \leq 0.02$ in inverse fits of the reflectance was sufficient for reconstruction of top layer scattering (μ'_{s_1}) and the bottom layer absorption (μ_{a_2}) with mean errors of lesser than 5% (for μ_{a_2}) and lower than 3% (for μ'_{s_1}), across all SDS tested and as shown in figures 2(b)-(c) A1(b)-(c) and A2(b)-(c). However, the scattering of the bottom layer (μ'_{s_2}) could not be reconstructed accurately and showed average error of more than 60% across all SDS, indicating layered DT is largely unperturbed by changes in deep-layer scattering, as reported before [7,18,39,50,51]. Although recovery of top layer absorption μ_{a_1} was achieved, it was inconsistent, with mean errors $\leq$ 15% for all 384 models

 doi:10.20944/preprints202505.1896.v1

at SDS = 1.5 and 2 cm that increased to more than 50 % for SDS of 2.5 cm, which indicates that the reconstruction upper layer absorption was highly sensitive to SNR.

The input coefficients for each tissue model simulated here were obtained by assuming only two chromophores ($[dHb]$ and $[HbO]$) were present in each layer, the values are shown in Table 1. In the inverse sense, these chromophore concentrations had to be obtained from reconstructed absorption coefficients, for each layer, at each wavelength. Thus, as expected, errors in recovery of μ_{a_1} impacted the estimation of oxygenated and deoxygenated hemoglobin concentrations for the upper layer, with mean error being higher than $5 \pm 2\mu$M but lower than $10 \pm 3\mu$M for SDS 1.5 and 2 cm (Figure 3(a)-(b) and Figure A3(a)-(b)). The upper bound on of top-layer concentration errors grew to more than 15μM for both chromophore concentrations at SDS of 2.5 cm (A4(a)-(b)). The bottom-layer reconstructions demonstrated good agreement with ground truth values (to better than 3 μM at all SDS) while also having low inter-model variance.

Accurate recovery of individual chromophore concentrations is important, as clinically relevant parameters such as oxygen saturation (SO_2) and total hemoglobin concentration ($[THb]$) are derived from the combined contributions of $[HbO]$ and $[dHb]$ as markers of tissue health and metabolic demand. Errors in reconstruction of the top layer chromophore concentrations thus impacted retrieval of top layer SO_2 (error > 5% for all SDS). The top layer $[THb]$ values were retrieved with mean errors greater than 15% for shorter SDS (1.5 and 2 cm), which increased to more than 70% for larger SDS (Figure 4(a)-(b)). Again, this is consistent with the idea that the diffuse reflectance collected at larger SDS would be most insensitive to upper layer optical coefficients.

These results highlight that bilayered DT has reduced sensitivity to the top layer absorption and reconstruction of μ_{a_1} is sensitive to signal quality. However, recovery of bottom layer endpoints was accurate with SO_2 and $[ThB]$ being estimated to better than 3% across all SDS. This result is particularly encouraging since it signifies that real-world applications could enhance the quantitative sensitivity of functional properties recovered from deeper tissue layers, while being immune to changes in superficial layers, by using improved analytical models for reconstruction of TD reflectance [11,53,54].

A practical consideration that remained significant was the computational cost involved with reconstructions using the bilayer inverse model. The inverse fits converged in under 100 milliseconds using the analytical DT expression for a SI model, while for bilayer reconstructions inverse fits were approximately three orders of magnitude slower (taking about 150 s for each model). All inverse calculations were run on nodes of a high-performance computing cluster (with each node having an Intel Xeon Gold processor). For the 384 models analyzed at 3 SDS, the total computation time was almost 40 CPU-hours. This disparity presents a significant bottleneck for real-time or high-throughput analysis and motivates the development of computationally efficient strategies or machine-learning based models for acceleration.

Ultimately, the computational costs were recovered by the layered model as it consistently outperformed the semi-infinite model in terms of accuracy to recover μ_{a_2} and μ'_{s_1} even at large SDS (Figure 5 and Figure A5). On average the bilayered modeling performed about 10 - 15% better than SI model, across optical coefficients (except μ'_{s_2}) at SDS = 1.5 and 2 cm. It is interesting to note that bilayered DT models could extract μ_{a_2} accurately, even for shorter SDS could prove to be practically useful, as shorter SDS channels usually have better SNR.

5. Conclusions

We showed that using multi-layer DT for analysis of TD reflectance in bilayered media allowed for quantitative reconstruction of optical absorption of both layers with errors well within requisite thresholds for clinical utility. 64 different head and limb models at three commonly used near infrared wavelengths were used to simulate a total of 384 MC reflectance signals used for our analysis. For the top layer, absorption coefficient (μ_{a_1}) was reconstructed with mean errors < 0.03 cm^{-1} at SDS = 1.5 and 2 cm (rising to $\gtrsim 0.1$ cm^{-1} at 2.5 cm), while reduced scattering coefficient (μ'_{s_1}) showed high accuracy (< 2 cm^{-1} across all SDS). Bottom layer absorption, μ_{a_2} on the other hand was retrieved

 doi:10.20944/preprints202505.1896.v1

exceptionally well (< 0.01 cm^{-1} error) while bottom layer scattering μ'_{s_2} could not be well estimated. These translated to errors in biomarkers with top-layer $[THb]$ and SO_2 values having larger errors relative to the bottom-layer, highlighting the utility of layered DT to assess depth-resolved tissue physiology. Layered DT always outperformed semi-infinite DT, across all retrieved optical coefficients but had significantly higher computational costs. Future work will investigate approaches to reduce computational time for optimization, for e.g., by using SI DT to bootstrap the optimization, or to exclude μ'_{s_2} reconstructions. Approaches that reduce dimensionality of the inverse problem could potentially accelerate reconstructions without sacrificing accuracy.

Author Contributions: Conceptualization, S.R. and K.V; methodology, S.R. and K.V; software, S.R.; validation, S.R. and K.V.; investigation, S.R.; writing—original draft preparation, S.R.; writing—review and editing, S.R. and K.V.; visualization, S.R.; supervision, K.V.; All authors have read and agreed to the published version of the manuscript.

Funding: This research received no external funding

Institutional Review Board Statement: Not applicable

Data Availability Statement: LightPropagation.jl is a registered Julia package that can be installed on a Julia version > 1.5. The MC simulations and inverse fitting codes are available on request .

Acknowledgments: This work builds upon the computational advancements of Dr. Michael Helton (University of Michigan), developer of LightPropagation.jl – a Julia-based toolbox for solving time-resolved photon migration in turbid media . We also thank Dr. Jens Müller for facilitating high-performance simulations on the Miami Redhawk cluster.

Conflicts of Interest: "The authors declare no conflicts of interest."

Abbreviations

The following abbreviations are used in this manuscript:

SI	Semi Infinite
DT	Diffusion Theory
MC	Monte Carlo
TPSF	Temporal Point Spread Function
THb	Total Hemoglobin Concentration
SO_2	Fractional Oxygen Saturation
SDS	Source Detector Separation
SNR	Signal to Noise Ratio

Appendix A. Computed optical transport coefficients

Here we report the computed optical coefficients using the ranges for SO_2 and $[THb]$ described in Table 1.

Table A1. The selected target tissue properties. The values below were calculated for $\lambda = 690$ nm. The value reported for each optical property is the mean of the coefficients (4 for absorption for each layer and 2 for scattering for ech layer) along with the range covering all the computed values. The coefficient values used for our analysis for each model, however were not evenly spread within this range.

Tissue Model	Layer	$\mu_a\ cm^{-1}$	$\mu_{sp}\ cm^{-1}$
Head	Top (scalp,skull)	0.079 ± 0.091	13.329 ± 4.251
	Bottom (Brain)	0.106 ± 0.055	14.810 ± 0.271
Muscle	Top (skin,fat)	0.074 ± 0.090	18.854 ± 6.752
	Bottom (Muscle)	0.088 ± 0.046	6.822 ± 2.844

 doi:10.20944/preprints202505.1896.v1

Table A2. The values below were calculated for $\lambda = 760$ nm.

Tissue Model	Layer	$\mu_a\ cm^{-1}$	$\mu_{sp}\ cm^{-1}$
Head	Top (scalp,skull)	0.096 ± 0.072	12.823 ± 3.868
	Bottom (Brain)	0.107 ± 0.046	12.068 ± 0.88
Muscle	Top (skin,fat)	0.080 ± 0.070	17.467 ± 5.807
	Bottom (Muscle)	0.087 ± 0.036	5.939 ± 2.905

Table A3. The values below were calculated for $\lambda = 850$ nm.

Tissue Model	Layer	$\mu_a\ cm^{-1}$	$\mu_{sp}\ cm^{-1}$
Head	Top (scalp,skull)	0.120 ± 0.062	12.267 ± 3.451
	Bottom (Brain)	0.104 ± 0.038	9.619 ± 1.702
Muscle	Top (skin,fat)	0.086 ± 0.057	16.003 ± 4.835
	Bottom (Muscle)	0.081 ± 0.028	5.098 ± 2.880

Appendix B. Reconstruction of Optical Coefficients

The optical coefficients recovered across all source-detector separations exhibited consistent recovery accuracy trends across all wavelengths as described above. Figures A1 and A2 illustrate the reconstruction of the optical coefficients at wavelengths of 690 nm and 850 nm, respectively.

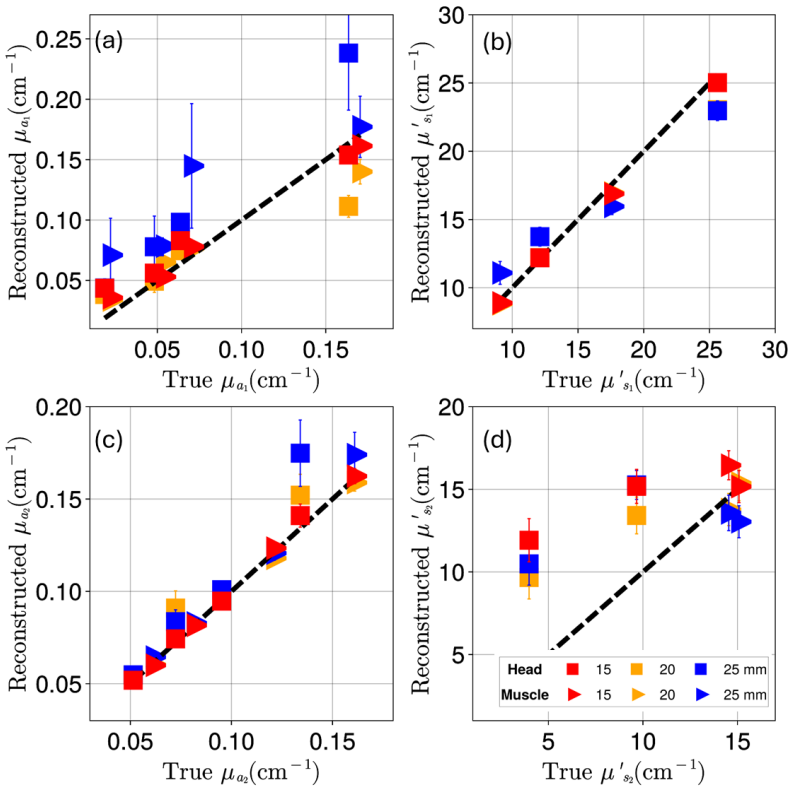

Figure A1. True versus reconstructed transport coefficients at 690 nm

 doi:10.20944/preprints202505.1896.v1

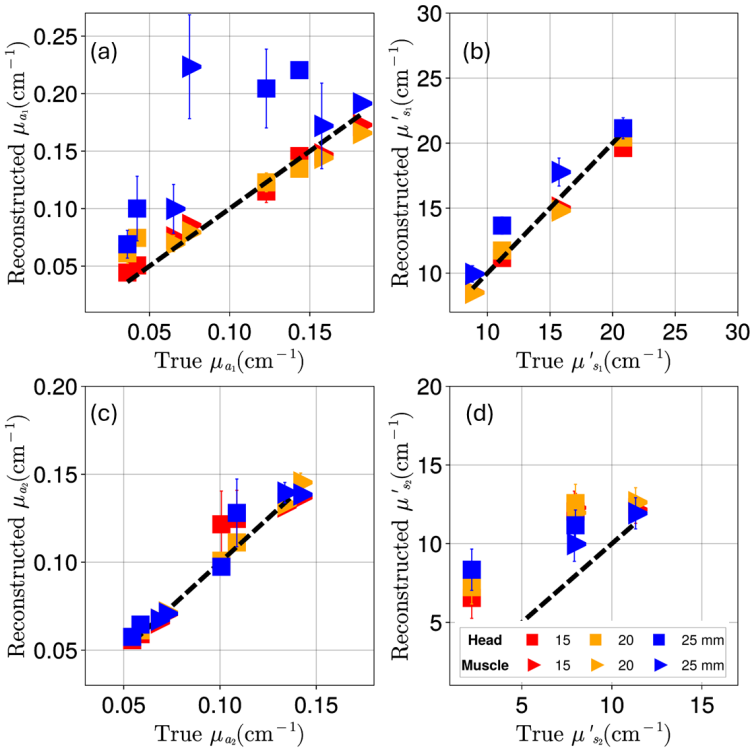

Figure A2. True versus reconstructed transport coefficients at 850 nm

Appendix C. Reconstruction of Deoxygenated and Oxygenated Hemoglobin Concentrations

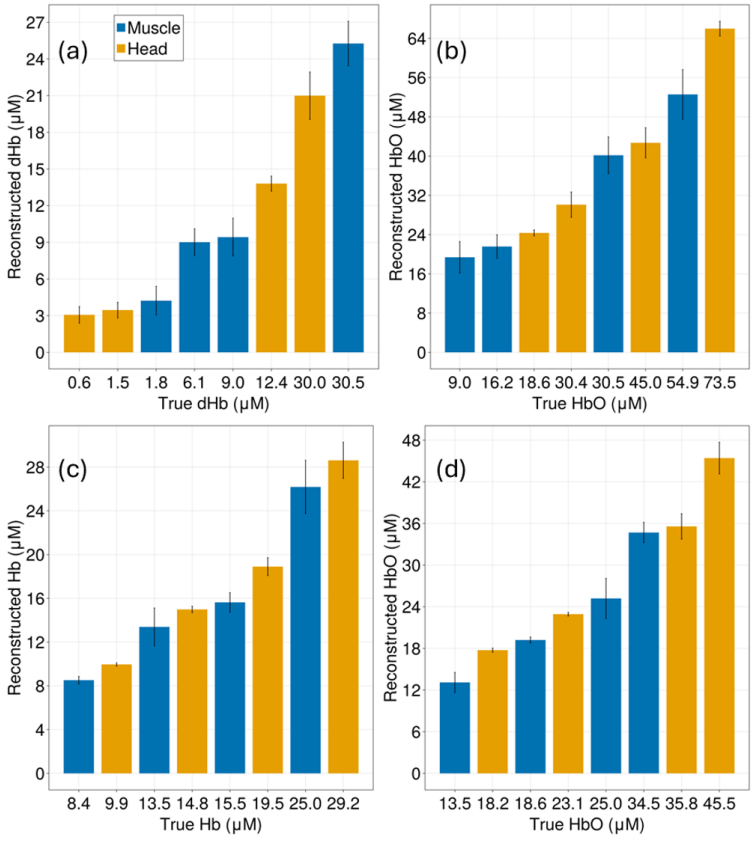

Figure A3. The reconstructed chromophore concentrations at 2 cm. Here, similar to Figure 3, the x-axis is not evenly spaced to avoid sparsely populated graph.

 doi:10.20944/preprints202505.1896.v1

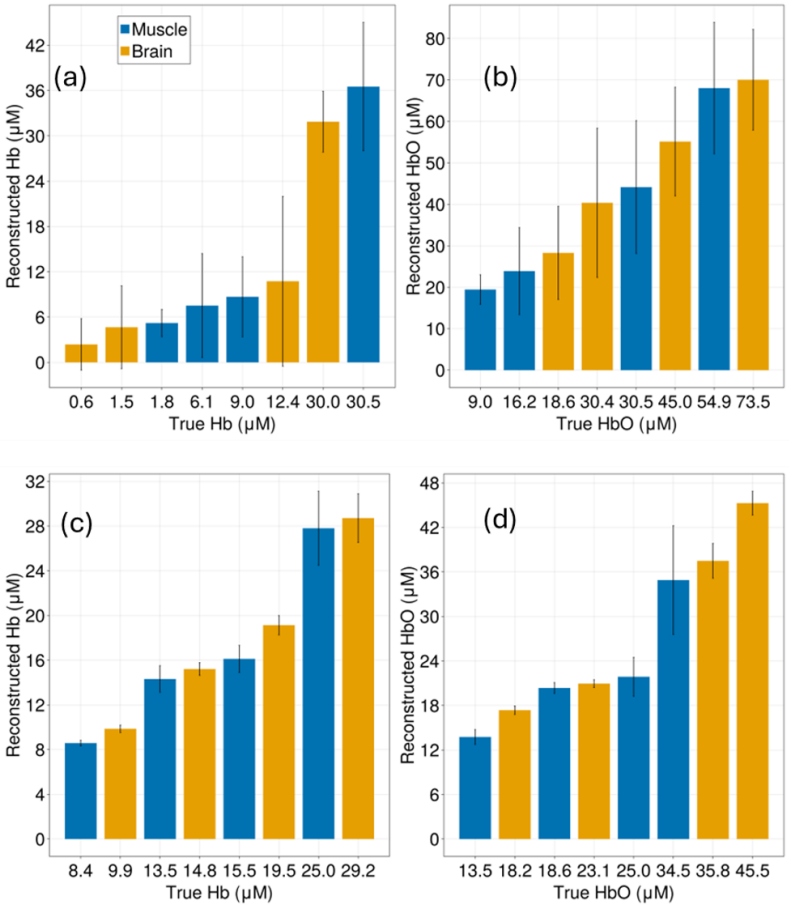

Figure A4. The reconstructed chromophore concentration at 2.5 cm. The notable difference here being the increased error in retrieval of the top layer concentrations.

Appendix D. Reconstruction of Optical Coefficients Using Semi-Infinite Tissue Approximation

Semi

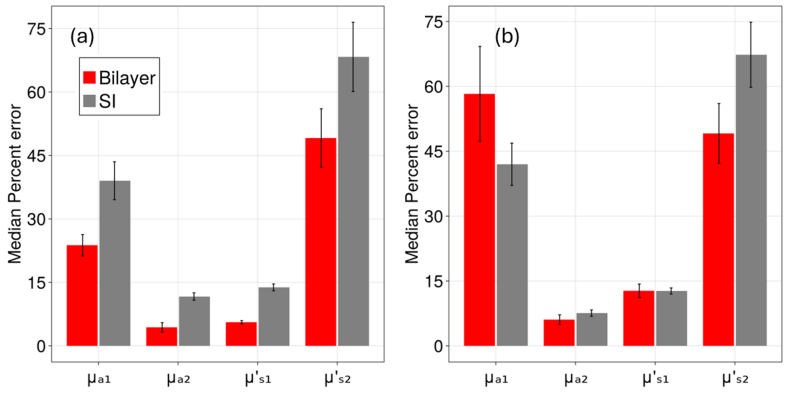

Figure A5. Comparison of percent errors in the reconstructed optical properties for the bilayered and semi-infinite (SI) models. The sub-figures **(a)** and **(b)**, correspond to SDS = 2 and 2.5 cm respectively. The optical properties analyzed include the absorption coefficients of the first and second layers (μ_{a_1}, μ_{a_2}) and the reduced scattering coefficients of the first and second layers (μ'_{s_1}, μ'_{s_2}) labeled as groups along the x-axis.

References

1. Blaney, G.; Donaldson, R.; Mushtak, S.; Nguyen, H.; Vignale, L.; Fernandez, C.; Pham, T.; Sassaroli, A.; Fantini, S. Dual-Slope Diffuse Reflectance Instrument for Calibration-Free Broadband Spectroscopy. *Applied Sciences* **2021**, *11*. https://doi.org/10.3390/app11041757.

 doi:10.20944/preprints202505.1896.v1

2. Shimada, M.; Hoshi, Y.; Yamada, Y. Simple algorithm for the measurement of absorption coefficients of a two-layered medium by spatially resolved and time-resolved reflectance. *Applied Optics* **2005**, *44*, 7554. https://doi.org/10.1364/AO.44.007554.
3. Sekar, S.K.V.; Lanka, P.; Farina, A.; Mora, A.D.; Andersson-Engels, S.; Taroni, P.; Pifferi, A. Broadband Time Domain Diffuse Optical Reflectance Spectroscopy: A Review of Systems, Methods, and Applications. *Applied Sciences 2019, Vol. 9, Page 5465* **2019**, *9*, 5465. https://doi.org/10.3390/APP9245465.
4. Ugai, T.; Sasamoto, N.; Lee, H.Y.; Ando, M.; Song, M.; Tamimi, R.M.; Kawachi, I.; Campbell, P.T.; Giovannucci, E.L.; Weiderpass, E.; et al. Is early-onset cancer an emerging global epidemic? Current evidence and future implications. https://doi.org/10.1038/s41571-022-00672-8.
5. Ferrari, M.; Quaresima, V. A brief review on the history of human functional near-infrared spectroscopy (fNIRS) development and fields of application. *NeuroImage* **2012**, *63*, 921–35. https://doi.org/10.1016/j.neuroimage.2012.03.049.
6. Yamada, Y.; Suzuki, H.; Yamashita, Y. Time-Domain Near-Infrared Spectroscopy and Imaging: A Review. *Applied Sciences* **2019**, *9*. https://doi.org/10.3390/app9061127.
7. Pifferi, A.; Contini, D.; Mora, A.D.; Farina, A.; Spinelli, L.; Torricelli, A. New frontiers in time-domain diffuse optics, a review. *Journal of Biomedical Optics* **2016**, *21*, 091310. https://doi.org/10.1117/1.jbo.21.9.091310.
8. Boer, L.L.D.; Bydlon, T.M.; Duijnhoven, F.V.; Peeters, M.J.T.V.; Loo, C.E.; Winter-Warnars, G.A.; Sanders, J.; Sterenborg, H.J.; Hendriks, B.H.; Ruers, T.J. Towards the use of diffuse reflectance spectroscopy for real-time in vivo detection of breast cancer during surgery. *Journal of Translational Medicine* **2018**, *16*, 1–14. https://doi.org/10.1186/s12967-018-1747-5.
9. Hallacoglu, B. Absolute measurement of cerebral optical coefficients, hemoglobin concentration and oxygen saturation in old and young adults with near-infrared spectroscopy. *Journal of Biomedical Optics* **2012**, *17*, 081406. https://doi.org/10.1117/1.JBO.17.8.081406.
10. Farina, A.; Torricelli, A.; Bargigia, I.; Spinelli, L.; Cubeddu, R.; Foschum, F.; Jäger, M.; Simon, E.; Fugger, O.; Kienle, A.; et al. In-vivo multilaboratory investigation of the optical properties of the human head. *Biomedical Optics Express* **2015**, *6*, 2609. https://doi.org/10.1364/BOE.6.002609.
11. Calcaterra, V.; Lacerenza, M.; Amendola, C.; Buttafava, M.; Contini, D.; Rossi, V.; Spinelli, L.; Zanelli, S.; Zuccotti, G.; Torricelli, A. Cerebral baseline optical and hemodynamic properties in pediatric population: a large cohort time-domain near-infrared spectroscopy study. *Neurophotonics* **2024**, *11*. https://doi.org/10.1117/1.NPh.11.4.045009.
12. Bossi, A.; Bianchi, L.; Saccomandi, P.; Pifferi, A. Optical signatures of thermal damage on ex-vivo brain, lung and heart tissues using time-domain diffuse optical spectroscopy. *Biomedical Optics Express* **2024**, *15*, 2481. https://doi.org/10.1364/boe.517376.
13. Martelli, F.; Binzoni, T.; Bianco, S.D.; Liemert, A.; Kienle, A. *Light Propagation Through Biological Tissue and Other Diffusive Media_ Theory, Solutions, and Validations*; SPIE, 2022.
14. Hoshi, Y. *New Horizons in Time-Domain Diffuse Optical Spectroscopy and Imaging*; MDPI, 2020.
15. Blaney, G.; Sassaroli, A.; Fantini, S. Spatial sensitivity to absorption changes for various near-infrared spectroscopy methods: A compendium review. *Journal of Innovative Optical Health Sciences* **2024**. https://doi.org/10.1142/S1793545824300015.
16. Wada, H.; Yoshizawa, N.; Ohmae, E.; Ueda, Y.; Yoshimoto, K.; Mimura, T.; Nasu, H.; Asano, Y.; Ogura, H.; Sakahara, H.; et al. Water and lipid content of breast tissue measured by six-wavelength time-domain diffuse optical spectroscopy. *Journal of Biomedical Optics* **2022**, *27*. https://doi.org/10.1117/1.JBO.27.10.105002.
17. Tagliabue, S.; Kacprzak, M.; Rey-Perez, A.; Baena, J.; Riveiro, M.; Maruccia, F.; Fischer, J.B.; Poca, M.A.; Durduran, T. How the heterogeneity of the severely injured brain affects hybrid diffuse optical signals: case examples and guidelines. *Neurophotonics* **2024**, *11*. https://doi.org/10.1117/1.NPh.11.4.045005.
18. Kienle, A.; Glanzmann, T.; Wagnières, G.; van den Bergh, H. Investigation of two-layered turbid media with time-resolved reflectance. *Applied Optics* **1998**, *37*, 6852. https://doi.org/10.1364/AO.37.006852.
19. Taroni, P.; Pifferi, A.; Quarto, G.; Farina, A.; Ieva, F.; Paganoni, A.M.; Abbate, F.; Cassano, E.; Cubeddu, R. Time domain diffuse optical spectroscopy: in-vivo quantification of collagen in breast tissue. In Proceedings of the Optical Methods for Inspection, Characterization, and Imaging of Biomaterials II. SPIE, 2015, Vol. 9529, pp. 140–147.
20. Pellicer, A.; del Carmen Bravo, M. Near-infrared spectroscopy: A methodology-focused review. *Seminars in Fetal and Neonatal Medicine* **2011**, *16*, 42–49. https://doi.org/10.1016/J.SINY.2010.05.003.

 doi:10.20944/preprints202505.1896.v1

21. Vera, D.A.; García, H.A.; Waks-Serra, M.V.; Carbone, N.A.; Iriarte, D.I.; Pomarico, J.A. Determining light absorption changes in multilayered turbid media through analytically computed photon mean partial pathlengths. *Optica Pura y Aplicada* **2023**, *56*. https://doi.org/10.7149/OPA.56.2.51145.
22. Hielscher, A.H.; Liu, H.; Chance, B.; Tittel, F.K.; Jacques, S.L. Time-resolved photon emission from layered turbid media. *Applied Optics* **1996**, *35*, 719. https://doi.org/10.1364/AO.35.000719.
23. Lanka, P.; Segala, A.; Farina, A.; Sekar, S.K.V.; Nisoli, E.; Valerio, A.; Taroni, P.; Cubeddu, R.; Pifferi, A. Non-invasive investigation of adipose tissue by time domain diffuse optical spectroscopy. *Biomedical Optics Express* **2020**, *11*, 2779. https://doi.org/10.1364/BOE.391028.
24. Giovannella, M.; Contini, D.; Pagliazzi, M.; Pifferi, A.; Spinelli, L.; Erdmann, R.; Donat, R.; Rocchetti, I.; Rehberger, M.; Konig, N.; et al. BabyLux device: a diffuse optical system integrating diffuse correlation spectroscopy and time-resolved near-infrared spectroscopy for the neuromonitoring of the premature newborn brain. *Neurophotonics* **2019**, *6*, 1. https://doi.org/10.1117/1.NPh.6.2.025007.
25. Jones, Z.D.; Reitzle, D.; Kienle, A. Errors in diffuse optical absorption spectroscopy of two-layered turbid media due to assuming a homogeneous medium. *Opt. Lett.* **2025**, *50*, 3118–3121. https://doi.org/10.1364/OL.562315.
26. Ferrari, M.; Quaresima, V. Near Infrared Brain and Muscle Oximetry: From the Discovery to Current Applications. *Journal of Near Infrared Spectroscopy* **2012**, *20*, 1–14. https://doi.org/10.1255/jnirs.973.
27. Helton, M.; Zerafa, S.; Vishwanath, K.; Mycek, M.A. Efficient computation of the steady-state and time-domain solutions of the photon diffusion equation in layered turbid media. *Sci. Rep.* **2022**, *12*, 18979.
28. Jacques, S.L. Optical properties of biological tissues: a review. *Physics in Medicine & Biology* **2013**, *58*, R37. https://doi.org/10.1088/0031-9155/58/11/R37.
29. Gagnon, L.; Gauthier, C.; Hoge, R.D.; Lesage, F.; Selb, J.; Boas, D.A. Double-layer estimation of intra- and extracerebral hemoglobin concentration with a time-resolved system. *Journal of Biomedical Optics* **2008**, *13*, 054019. https://doi.org/10.1117/1.2982524.
30. Shimada, M.; Hoshi, Y.; Yamada, Y. Simple algorithm for the measurement of absorption coefficients of a two-layered medium by spatially resolved and time-resolved reflectance. *Appl. Opt.* **2005**, *44*, 7554–7563. https://doi.org/10.1364/AO.44.007554.
31. Sato, C.; Shimada, M.; Yamada, Y.; Hoshi, Y. Extraction of depth-dependent signals from time-resolved reflectance in layered turbid media. *Journal of Biomedical Optics* **2005**, *10*, 064008. https://doi.org/10.1117/1.2136312.
32. Sharma, M.; Hennessy, R.; Markey, M.K.; Tunnell, J.W. Verification of a two-layer inverse Monte Carlo absorption model using multiple source-detector separation diffuse reflectance spectroscopy. *Biomedical Optics Express* **2014**, *5*, 40. https://doi.org/10.1364/boe.5.000040.
33. Blaney, G.; Bottoni, M.; Sassaroli, A.; Fernandez, C.; Fantini, S. Broadband diffuse optical spectroscopy of two-layered scattering media containing oxyhemoglobin, deoxyhemoglobin, water, and lipids. *Journal of Innovative Optical Health Sciences* **2022**, *15*. https://doi.org/10.1142/S1793545822500201.
34. Sato, C.; Shimada, M.; M.D., Y.H.; Yamada, Y. Extraction of depth-dependent signals from time-resolved reflectance in layered turbid media. *Journal of Biomedical Optics* **2005**, *10*, 064008. https://doi.org/10.1117/1.2136312.
35. Steinbrink, J.; Wabnitz, H.; Obrig, H.; Villringer, A.; Rinneberg, H. Determining changes in NIR absorption using a layered model of the human head. *Physics in Medicine and Biology* **2001**, *46*, 879–896. https://doi.org/10.1088/0031-9155/46/3/320.
36. Kienle, A.; Patterson, M.S.; Dögnitz, N.; Bays, R.; Wagnières, G.; van den Bergh, H. Noninvasive determination of the optical properties of two-layered turbid media. *Applied Optics* **1998**, *37*, 779. https://doi.org/10.1364/AO.37.000779.
37. Kienle, A.; Patterson, M.S. Improved solutions of the steady-state and the time-resolved diffusion equations for reflectance from a semi-infinite turbid medium. *Journal of the Optical Society of America A* **1997**, *14*, 246. https://doi.org/10.1364/JOSAA.14.000246.
38. Tualle, J.M.; Prat, J.; Tinet, E.; Avrillier, S. Real-space Green's function calculation for the solution of the diffusion equation in stratified turbid media. *Journal of the Optical Society of America A* **2000**, *17*, 2046. https://doi.org/10.1364/JOSAA.17.002046.
39. Martelli, F.; Pifferi, A.; Farina, A.; Amendola, C.; Maffeis, G.; Tommasi, F.; Cavalieri, S.; Spinelli, L.; Torricelli, A. Statistics of maximum photon penetration depth in a two-layer diffusive medium. *Biomedical Optics Express* **2024**, *15*, 1163. https://doi.org/10.1364/BOE.507294.

 doi:10.20944/preprints202505.1896.v1

40. Martelli, F.; Sassaroli, A.; Yamada, Y.; Zaccanti, G. Analytical approximate solutions of the time-domain diffusion equation in layered slabs. *Journal of the Optical Society of America. A, Optics, image science, and vision* **2002**, *19 1*, 71–80.
41. García, H.; Iriarte, D.; Pomarico, J.; Grosenick, D.; Macdonald, R. Retrieval of the optical properties of a semiinfinite compartment in a layered scattering medium by single-distance, time-resolved diffuse reflectance measurements. *Journal of Quantitative Spectroscopy and Radiative Transfer* **2017**, *189*, 66–74. https://doi.org/10.1016/j.jqsrt.2016.11.018.
42. Wu, M.M.; Chan, S.T.; Mazumder, D.; Tamborini, D.; Stephens, K.A.; Deng, B.; Farzam, P.; Chu, J.Y.; Franceschini, M.A.; Qu, J.Z.; et al. Improved accuracy of cerebral blood flow quantification in the presence of systemic physiology cross-talk using multi-layer Monte Carlo modeling. *Neurophotonics* **2021**, *8*. https://doi.org/10.1117/1.NPh.8.1.015001.
43. Martelli, F.; Sassaroli, A.; Bianco, S.D.; Yamada, Y.; Zaccanti, G. Solution of the time-dependent diffusion equation for layered diffusive media by the eigenfunction method. *Physical Review E* **2003**, *67*, 056623. https://doi.org/10.1103/PhysRevE.67.056623.
44. Helton, M. LightPropagation.jl: A Julia package for simulating light propagation, 2025. Accessed: 2025-03-15.
45. McMurdy, J.; Jay, G.; Suner, S.; Crawford, G. Photonics-based In Vivo total hemoglobin monitoring and clinical relevance. *Journal of Biophotonics* **2009**, *2*, 277–287. https://doi.org/10.1002/jbio.200910019.
46. Prahl, S. Optical Absorption Spectra of Hemoglobin. https://omlc.org/spectra/hemoglobin/summary.html, 1999. Accessed: October 15, 2023. Oregon Medical Laser Center.
47. Vishwanath, K.; Pogue, B.; Mycek, M.A. Quantitative fluorescence lifetime spectroscopy in turbid media: comparison of theoretical, experimental and computational methods. *Physics in Medicine & Biology* **2002**, *47*, 3387. https://doi.org/10.1088/0031-9155/47/18/308.
48. Vishwanath, K.; Mycek, M.A. Time-resolved photon migration in bi-layered tissue models. *Optics Express* **2005**, *13*, 7466. https://doi.org/10.1364/OPEX.13.007466.
49. Khan, R.; Gul, B.; Khan, S.; Nisar, H.; Ahmad, I. Refractive index of biological tissues: Review, measurement techniques, and applications. *Photodiagnosis and Photodynamic Therapy* **2021**, *33*, 102192. https://doi.org/10.1016/j.pdpdt.2021.102192.
50. Martelli, F.; Bianco, S.D.; Zaccanti, G.; Pifferi, A.; Torricelli, A.; Bassi, A.; Taroni, P.; Cubeddu, R. Phantom validation and in vivo application of an inversion procedure for retrieving the optical properties of diffusive layered media from time-resolved reflectance measurements. *Optics Letters* **2004**, *29*, 2037. https://doi.org/10.1364/OL.29.002037.
51. Rajasekhar, S.; Vishwanath, K. Sensitivity Of Time-Resolved Diffuse Reflectance To Optical Coefficients In Bilayered Tissues. In Proceedings of the Frontiers in Optics + Laser Science 2024 (FiO, LS). Optica Publishing Group, 2024, p. JW5A.45. https://doi.org/10.1364/FIO.2024.JW5A.45.
52. Stawschenko, E.; Schaller, T.; Kern, B.; Bode, B.; Dörries, F.; Kusche-Vihrog, K.; Gehring, H.; Wegerich, P. Current Status of Measurement Accuracy for Total Hemoglobin Concentration in the Clinical Context. *Biosensors* **2022**, *12*. https://doi.org/10.3390/bios12121147.
53. Nasseri, N.; Kleiser, S.; Ostojic, D.; Karen, T.; Wolf, M. Quantifying the effect of adipose tissue in muscle oximetry by near infrared spectroscopy. *Biomedical Optics Express* **2016**, *7*, 4605. https://doi.org/10.1364/BOE.7.004605.
54. Dehaes, M.; Grant, P.E.; Sliva, D.D.; Roche-Labarbe, N.; Pienaar, R.; Boas, D.A.; Franceschini, M.A.; Selb, J. Assessment of the frequency-domain multi-distance method to evaluate the brain optical properties: Monte Carlo simulations from neonate to adult. *Biomedical Optics Express* **2011**, *2*, 552. https://doi.org/10.1364/BOE.2.000552.